



HAL
open science

The HDO cycle on Mars: Comparison of ACS observations with GCM simulations

Loïc Rossi, Margaux Vals, Juan Alday, Franck Montmessin, Anna Fedorova, Alexander Trokhimovskiy, Oleg Korablev, Franck Lefèvre, Francisco Gonzalez-Galindo, Mikhail Luginin, et al.

► To cite this version:

Loïc Rossi, Margaux Vals, Juan Alday, Franck Montmessin, Anna Fedorova, et al.. The HDO cycle on Mars: Comparison of ACS observations with GCM simulations. *Journal of Geophysical Research. Planets*, 2022, 127 (8), pp.e2022JE007201. 10.1029/2022JE007201 . insu-03740469

HAL Id: insu-03740469

<https://insu.hal.science/insu-03740469v1>

Submitted on 21 Jul 2023

HAL is a multi-disciplinary open access archive for the deposit and dissemination of scientific research documents, whether they are published or not. The documents may come from teaching and research institutions in France or abroad, or from public or private research centers.

L'archive ouverte pluridisciplinaire **HAL**, est destinée au dépôt et à la diffusion de documents scientifiques de niveau recherche, publiés ou non, émanant des établissements d'enseignement et de recherche français ou étrangers, des laboratoires publics ou privés.

Copyright

This article is a companion to Vals et al. (2022), <https://doi.org/10.1029/2022JE007192>.

Special Section:

ExoMars Trace Gas Orbiter - One Martian Year of Science

Key Points:

- We simulated the HDO cycle on Mars using a 3D Global Climate Model
- GCM simulations were compared with solar occultations from Atmospheric Chemistry Suite on board the Trace Gas Orbiter
- A good representation of the condensation processes is key to reproduce the observed D/H ratio

Correspondence to:












L. Rossi,
loic.rossi@latmos.ipsl.fr

Citation:

Rossi, L., Vals, M., Alday, J., Montmessin, F., Fedorova, A., Trokhimovskiy, A., et al. (2022). The HDO cycle on Mars: Comparison of ACS observations with GCM simulations. *Journal of Geophysical Research: Planets*, 127, e2022JE007201. <https://doi.org/10.1029/2022JE007201>

Received 25 JAN 2022
Accepted 21 JUN 2022

The HDO Cycle on Mars: Comparison of ACS Observations With GCM Simulations

Loïc Rossi¹ , Margaux Vals¹ , Juan Alday^{2,3} , Franck Montmessin¹ , Anna Fedorova⁴ , Alexander Trokhimovskiy⁴ , Oleg Korablev⁴ , Franck Lefèvre¹ , Francisco Gonzalez-Galindo⁵ , Mikhail Luginin⁴ , Antoine Bierjon⁶, François Forget⁶, and Ehouarn Millour⁶ 

¹LATMOS/IPSL, UVSQ Université Paris-Saclay, Sorbonne Université, CNRS, Guyancourt, France, ²AOPP, Department of Physics, University of Oxford, Oxford, UK, ³School of Physical Sciences, The Open University, Milton Keynes, UK, ⁴Space Research Institute (IKI), Moscow, Russia, ⁵Instituto de Astrofísica de Andalucía-CSIC (IAA), Granada, Spain, ⁶Laboratoire de Météorologie Dynamique (LMD/IPSL), Sorbonne Université, ENS, PSL Research University, Ecole Polytechnique, Institut Polytechnique de Paris, CNRS, Paris, France

Abstract The D/H ratio and its implications on the atmospheric escape, make it an essential observable to study the current and past inventory of water on Mars. With the arrival of the Trace Gas Orbiter around Mars, new measurements of the D/H ratio are now available and require tools to interpret the observations and understand the HDO cycle. We here present simulations of an updated version of the Laboratoire de Météorologie Dynamique Mars Global Climate Model which includes HDO and in particular the fractionation processes it undergoes. We compare our model simulations with the HDO observations in solar occultation from the Atmospheric Chemistry Suite mid-infrared channel on board the Trace Gas Orbiter (Alday et al., 2021; <https://doi.org/10.5281/ZENODO.5100448>). The model successfully reproduces the general trends of the D/H ratio, indicating that the main physical processes are captured by theory. A consistent simulation of condensation processes is found to be key in the representation of the D/H ratio. Improvements in the representation of clouds and on the water cycle will help improving the representation of the HDO cycle and better help extrapolate back in times the conditions of water escape on Mars.

Plain Language Summary Understanding how the Martian climate affects the isotopic ratio of water is key to understand the history of water on the planet. We use a general circulation model to simulate the cycle of HDO, an isotope of water, in the atmosphere of Mars. We compare our model results with spacecraft observations from the Atmospheric Chemistry Suite spectrometer on board the Trace Gas Orbiter, currently in orbit around Mars. Our model provides a good qualitative agreement with the observations. We find that the condensation of water vapor into ice is a critical process for determining the isotopic ratio of the vapor phase.

1. Introduction

The study of HDO is important to understand the history of water on Mars. The D/H ratio is an indicator of the escape of water, since D atoms are heavier and escape less easily than H atoms. Compared to the Earth value, the current D enrichment in H₂O isotopologues suggests water was initially 6 times more abundant on Mars than nowadays (Villanueva et al., 2015).

But different phenomena can modify the local D/H ratio. In particular, the vapor pressure isotope effect, that is caused by the lower vapor pressure of HDO compared to H₂O, leading to an enrichment of the ice phase in deuterium (Bertaux & Montmessin, 2001; Fouchet & Lellouch, 2000).

It is therefore important to model the HDO cycle in order to understand its transport and the physical processes affecting it. Previous theoretical work on Mars' HDO cycle was conducted by Bertaux and Montmessin (2001); Fouchet and Lellouch (2000) and a first implementation of HDO in a Global Climate Model (GCM) was described in Montmessin et al. (2005), using the Mars GCM from the Laboratoire de Météorologie Dynamique (LMD). With the Trace Gas Orbiter (TGO) mission, HDO has been profiled in altitude for the first time on Mars. These new data are of unprecedented value for constraining the processes at work that control the fate of HDO molecules in the atmosphere of Mars in comparison to that of water.

Rossi et al. (2021) (hereafter Rossi21) presented an updated version of the GCM used for the study of Montmessin et al. (2005). The model presented in Rossi21 was using a simplified cloud formation scheme, not taking into account the radiative effect of clouds nor the details of the microphysics. In Rossi21 we assessed the reimplementation by studying the effect on the HDO cycle and the D/H ratio of a scenario for dust opacity reproducing the dust conditions (through the dust column opacity) encountered during the Global Dust Storm of 2018 (martian year 34).

In this study we present an improved version of the model with respect to the one in Rossi21, and compare its predictions to observations in solar occultation performed by ACS onboard TGO. A companion paper (Vals et al., 2022 this issue) is dedicated to studying the impact of the different physical parametrizations affecting HDO on the D/H ratio.

We start by presenting the model, and in particular the representation of HDO, dust and clouds in the GCM (Section 2). This also includes the improvements to the model with respect to Rossi21. In Section 3 we present the data used for the comparison. We present the results of the model and compare them with the data in Section 4. We'll end with Section 5 for the discussion and conclusions.

2. Presentation of the Model

2.1. Representation of HDO

We use the Mars GCM from the LMD (Forget et al., 1999). In the model HDO is treated independently from H₂O with tracers following it under its vapor and ice phases, but also their amount on the surface.

Despite being independent tracers in the physical part of the model, HDO vapor and ice tracers are not transported independently by the dynamical part of the model. Instead, it is the isotopic ratio of the vapor or ice phase with respect to that of H₂O that is advected. This allows for the conservation of the ratio and reduces numerical errors. Details about this scheme can be found in Risi et al. (2010) and Rossi21.

The fractionation occurring at condensation is based on a fractionation factor that depends on the temperature, following Lamb et al. (2017):

$$\alpha(T) = \frac{(HDO/H_2O)_{ice}}{(HDO/H_2O)_{vap}} = \exp\left(\frac{13525}{T^2} - 5.59 \times 10^{-2}\right) \quad (1)$$

In Rossi21, this fractionation factor is used as such. However, considering that this improved version of the model includes detailed microphysics of cloud formation and interactions with dust which can lead to the presence of large supersaturations (Navarro et al., 2014), we also consider the effect of kinetics, with the formula derived by Jouzel and Merlivat (1984):

$$\alpha_c = \frac{\alpha(T)S}{\alpha(T) \times (D_{H_2O}/D_{HDO}) (S - 1) + 1} \quad (2)$$

where S is the water vapor saturation ratio, and D_{H_2O} and D_{HDO} are the diffusion coefficients for H₂O and HDO respectively. This means that the fractionation factor is made dependent on the saturation state of water vapor, which in turn means that supersaturation reduces the fractionation factor (cf. Vals et al., 2022 (this issue) for a detailed study on the effect of kinetics).

The amount of HDO being condensed in the ice is then given by:

$$dM_D = \alpha_c(T, S) dM_H \times \frac{M_D}{M_H} \quad (3)$$

where M indicates the mass in the vapor phase, dM the mass condensing, with subscript H referring to water and D to HDO.

Finally we also include in this study the effect of photochemistry. The chemical evolution of H₂O and HDO is calculated by the latest version of the photochemical module coupled to the LMD GCM, as described in Lefèvre et al. (2021). The photodissociation rates of HDO are based on the absorption cross-sections measured at 295 K

by Cheng et al. (2004) and Chung et al. (2001). For HDO the photolysis introduces another fractionation effect, opposite to that due to condensation, because the absorption cross-section of HDO in the UV is lower than that of H₂O. This process has little impact in the lower atmosphere, but is significant above 40 km, where H₂O and HDO are more intensely exposed to sunlight and are strongly photolyzed, in particular around perihelion. As discussed in the companion paper, including the photochemistry can increase the D/H ratio in the upper atmosphere, which is why we include it in this study.

2.2. Representation of Dust and Clouds

While Rossi21 was focused on the reimplementation of the HDO cycle described in Montmessin et al. (2005) in the LMD GCM, with simplified cloud physics, this study includes more physical processes in order to produce a more realistic HDO cycle, allowing comparisons with observations.

The water and dust cycles are following the settings and physical parametrizations described in Navarro et al. (2014). We use the two-moments scheme of Madeleine et al. (2011), in which the dust is fully described with two tracers: the dust mixing ratio and the dust number density. This scheme is said to be semi-interactive since the vertical distribution of the dust particles is free, but the optical depth of the column is constrained following dust scenarios based on observations (Montabone et al., 2015).

Regarding the cloud formation, Rossi21 used a simplified scheme in which all vapor above saturation was condensing. With the detailed microphysics of cloud formation, two additional tracers are considered to represent cloud condensation nuclei (CCN) mass and number density. This scheme also represents the interactions between clouds and dust (via nucleation and scavenging) which are tracked by the model thanks to the dedicated tracers. In this scheme, dust is necessary to provide CCN, which allows for the representation of the observed supersaturation conditions.

Finally this study also includes the radiative effect of the clouds (Madeleine et al., 2012; Navarro et al., 2014), which was absent from Rossi21. Including this effect globally warms up the middle atmosphere, reducing the condensation and the isotopic fractionation allowing for a higher D/H ratio above the cloud level. A detailed exploration on the influence of the radiative effect of clouds can be found in the companion paper Vals et al., 2022 (this issue).

2.3. Simulation Settings

The model is run using 64 cells in longitude (corresponding to 5.625° of longitude for each cell), 48 cells in latitude (3.75° each) and 32 vertical levels (up to ≈120 km). The physical timestep is 15 min, with a time-step of 30 s for the microphysical processes, which require a finer temporal resolution.

The initialization of the model starts with assuming a D/H ratio of 5 times the Earth's value (VSMOW [in the rest of the text, unless otherwise noted, all isotopic ratios are expressed in terms of VSMOW. $D/H_{VSMOW} = 1.5576 \times 10^{-4}$]) on the whole planet. The isotopic ratio of the perennial ice cap is set at a value of 5. The model is run using the “climatology” dust scenario for 10 years, in order to have a stabilized HDO cycle. This scenario represents the dust conditions of a typical martian year, without dust storm. Then the simulations are conducted using the scenarios for 2 years of interest: martian year 34 (MY34) during which occurred a global dust storm and martian year 35 (MY35). These reference dust scenarios are being provided by Montabone et al. (2020).

2.4. Comparison With Other Models

Besides the LMD Mars GCM used in Montmessin et al. (2005) and Rossi et al. (2021), there is another model in which the representation of HDO has been implemented, the GEM-Mars GCM. A recent study by Daerden et al. (2022) presents results of their implementation of the HDO cycle. We mention here some of the technical differences, which need to be taken into account prior to a comparison of the results from the two models.

The version of the GEM-Mars GCM used in Daerden et al. (2022) does not include the complete microphysics of cloud formation. In the LMD Mars GCM, the so-called “simplified” cloud formation scheme lead to excessive amounts of clouds near the poles. This excess of ice caused the model to be significantly too wet when the

radiative effect of clouds was taken into account. The implementation of the microphysical scheme was shown to solve the issue (Navarro et al., 2014). Daerden et al. (2022) solve this issue by prescribing a very large radius for ice particles over the north polar cap during summer, leading to a quick sedimentation of the particles. The ice radius being also prescribed in the rest of the atmosphere depending on the altitude range of the model grid cell.

In our model, the inclusion of the microphysics of cloud formation allows us to not put any restriction on the ice particle size, which is determined by the model itself based on the amount of ice and of available CCN (Madeleine et al., 2012; Montmessin et al., 2004).

Another important difference is the representation of the dust vertical distribution. In both the LMD Mars GCM and the GEM-Mars GCM, the total column opacity of dust is prescribed following the scenarios provided by Montabone et al. (2020), while the vertical distribution is free. As Neary et al. (2020) have shown, and as discussed in Rossi21, this representation is not capable of correctly representing the amount of dust particles at high altitude during the GDS of MY34. This is why Neary et al. (2020) and Daerden et al. (2022) use a prescribed dust profile, following a Conrath distribution.

Finally, the spin-up phase used by Daerden et al. (2022) starts from a dry atmosphere, with water only coming from the permanent northern cap, which has its isotopic ratio set to a higher value than ours (6 instead of 5).

3. Presentation of the Observations

The ExoMars TGO arrived to Mars on October 2016, and after an aerobraking phase, TGO lowered its altitude into its final orbit on March 2018, starting its science operations phase. The science payload of the ExoMars TGO comprises two spectrometers allowing the measurements of the D/H ratio: ACS (Atmospheric Chemistry Suite, Korablev et al. (2018)) and NOMAD (Nadir and Occultation for Mars Discovery, Vandaele et al. (2018)).

In this study, we compare the model simulations against the vertical profiles of different atmospheric parameters (i.e., temperature, water vapor mixing ratio and D/H ratio) measured by the mid-infrared channel (MIR) of the ACS reported in Alday et al. (2021). The analysis of the observations in Alday et al. (2021) focused in the ACS MIR solar occultations covering a spectral range between 2.65 and 2.77 μm , which correspond to approximately 14% of the total available number of observations. In total, the data set comprises 572 solar occultation observations expanding approximately 1.5 Martian Years, from $L_s = 165^\circ$ in MY34 to $L_s = 356^\circ$ in MY35. Due to the geometry of TGO's orbit, most of the solar occultations ($\sim 73\%$) occur at high latitudes ($\geq 45^\circ$) in both hemispheres, while latitudes in the range $45^\circ\text{S} - 45^\circ\text{N}$ are only sampled in approximately 27% of the observations.

The data products reported in Alday et al. (2021) comprise vertical profiles of pressure, temperature and water vapor mixing ratio up to ~ 100 km. On the other hand, the highest altitude at which the ACS measurements are sensitive to HDO and the D/H is largely dependent on the water abundance, varying seasonally from ~ 70 km close to perihelion, and ~ 30 km close to aphelion. On the other hand, the lowermost altitude of the retrieved profiles of all atmospheric parameters is largely dependent on the dust abundance, which also varies seasonally, being most prominent close to perihelion.

4. Results

4.1. General Trends in the Model

Figure 1 presents the seasonal evolution of the zonally averaged column quantities, for MY 34 and 35. The main features are the latitudinal variations: in the summer hemisphere, the sublimation of water from the polar regions releases water vapor along with HDO. The released vapor has an isotopic ratio of 5, the prescribed value for the isotopic ratio of the perennial ice. As observed in Rossi21, fractionation at condensation occurs in the polar winters, trapping HDO in the ice phase and therefore depleting the vapor phase and causing a strong decrease of the D/H ratio. Adding microphysics and the radiative effect of clouds has not altered significantly the cycle, although the transition between the high and low values of D/H is less abrupt in this simulation. In the simulations with simplified cloud physics (Rossi et al., 2021) the D/H ratio during the solstice season was quite stable from the summer pole down to the tropics in the winter hemisphere. In the simulations presented here, the decrease starts close to the equator with values down to ~ 4 , then decreasing further in the polar regions with ratios of ~ 3 .

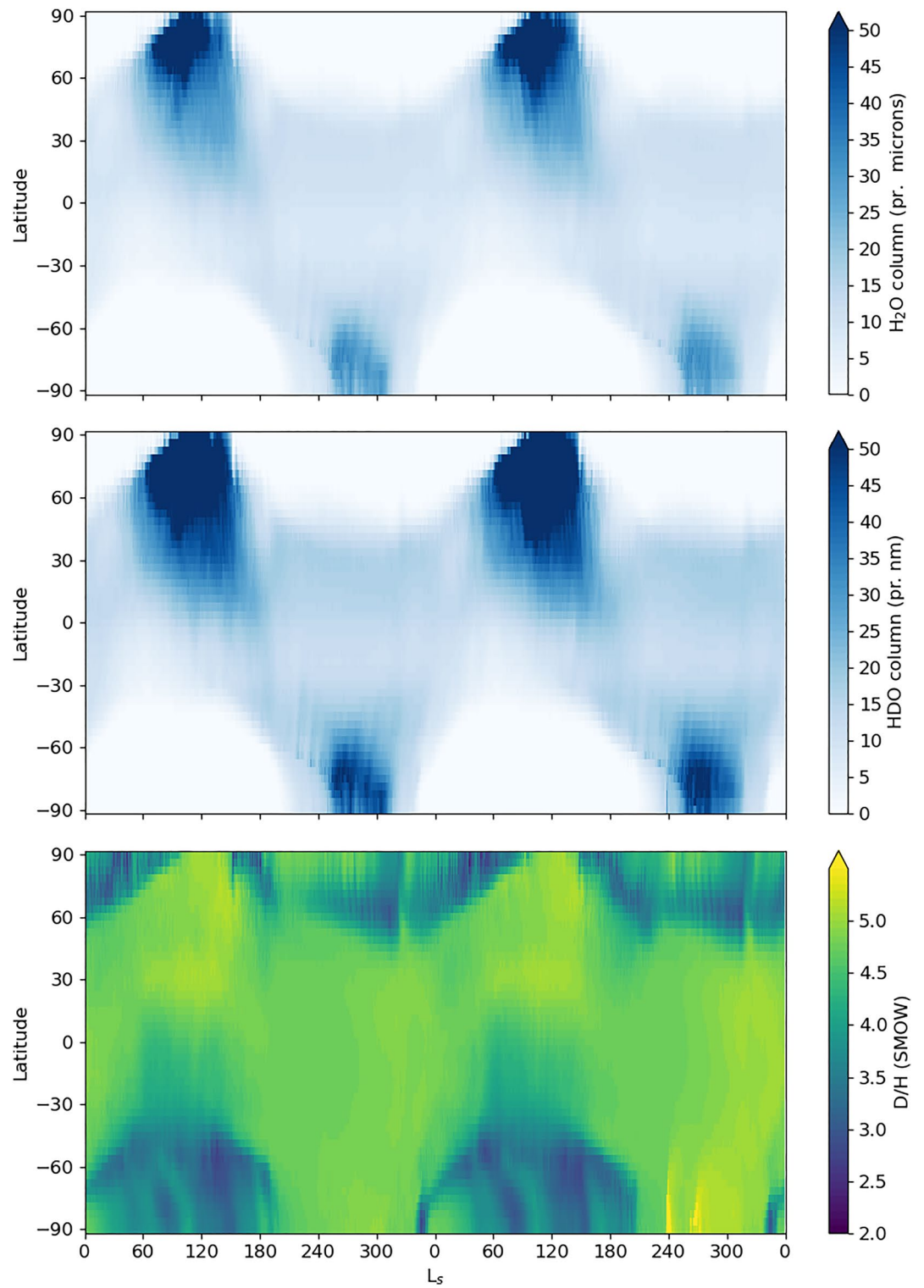


Figure 1. Simulated seasonal cycle of the zonal average, for the integrated column of H₂O vapor (top), HDO vapor (middle) and the associated D/H ratio (below), for MY34 and MY35.

As discussed in the companion paper Vals et al., 2022 (this issue), the minimum reached in the polar region is higher than with the simulation with simplified clouds, where it could go as low as ~ 1 .

As discussed in Rossi21 and in the companion paper, the global dust storm of MY34 has a strong effect on the distribution of deuterium in the atmosphere: it warms up the atmosphere, reducing the cloud formation and therefore the fractionation; it amplifies the atmospheric circulation, bringing more water vapor (and more HDO vapor) to higher altitudes.

This can clearly be seen in Figure 2 which shows the zonally averaged mixing ratio of HDO at an altitude of 30 and 60 km. We decide to define the deuteropause as the altitude above which the mixing ratio of HDO is lower than 50 ppb. If the whole vertical profile is lower than 50 ppb, then we consider that the deuteropause is not defined. This is a somewhat arbitrary, but consistent definition, allowing us to compare the latitudinal and seasonal evolution of the deuteropause, as in the lower panel of Figure 2, considering here the zonal average of the HDO vapor.

The effect of the dust storm is clearly visible in the model with a strong increase of the HDO mixing ratio at high altitude (here 60 km) around $L_s = 210^\circ$, during the peak of the dust storm of MY34. At the same period in MY35, an increase in the deuteropause altitude is visible, but is not as pronounced.

Figure 3 illustrates this effect on the D/H ratio, by comparing the two dust scenarios for MY34 and MY35. In both years, at $L_s = 180^\circ$ we can see the deuteropause as a strong decrease of the D/H ratio above the cloud formation region (around 30 km). At $L_s = 180^\circ$ the D/H ratio is already much higher above 70 km. This can be explained by an already weakened hygropause, with more water vapor reaching altitudes above 75 km in MY34 compared to MY35. This excess water vapor is photodissociated which strongly increases the isotopic ratio, even in areas with only a few ppm of water. As we move forward into the dust season, the martian year 34 stands out with clouds forming at much higher altitudes (>50 km) and a much higher D/H ratio above the clouds. As the dust storm decays, the cloud formation occurs at lower altitudes and the deuteropause becomes more effective, bringing the D/H ratio within similar values for the two scenarios. We can see here and in Figure 2 that the storm leaves the atmosphere relatively unperturbed below 30 km. Since most of atmospheric mass is located in the lower atmosphere, this explains why the D/H ratio of the column seems overall unaffected by the GDS in MY34 as seen in Figure 1.

This is similar to what was observed in Rossi21 and is illustrated in Figure 4: the radiative effect of clouds warms up the upper atmosphere and increases the strength of the circulation, allowing more water vapor to reach the upper atmosphere. The detailed microphysics of the cloud formation has the effect of reducing the amount of ice particles forming and allows for supersaturation. Both also favor a wetter upper atmosphere. In terms of D/H, the decreased efficiency of the hygropause also leads to less fractionation by condensation and therefore to a more porous deuteropause. In addition, the integration of the kinetics for the fractionation factor also leads to a weaker fractionation in the upper atmosphere. The net effect of these is to allow more HDO to go through the condensation area and to higher values of the D/H ratio.

A more detailed analysis of the effects of individual processes (microphysics, radiative effect of clouds and the supersaturation) can be found in the companion paper (Vals et al., 2022; this issue).

4.2. Comparison With Data

We now compare the H₂O and HDO profiles obtained from ACS MIR with the GCM simulations. The GCM outputs are colocated with the position (latitude and longitude) and date of the observations, after some processing.

The GCM simulations are first interpolated in terms of latitude, in order to increase the latitude resolution near the polar circle. This interpolation reduces errors in some cases where occultation coordinates would wrongly be considered in the polar night due to the model's coarse grid resolution. They are then interpolated in terms of solar zenith angle (SZA) to match the geometry of a solar occultation ($SZA = 90^\circ$). The observations and the GCM outputs are also resampled on a vertical grid of 100 points between -1 and 100 km above the areoid, facilitating the comparison.

Figure 5 shows the comparison of ACS with GCM profiles for the temperature. The model reproduces well the trends seen in the observations, but it also presents many areas in which it is warmer than the observations. In

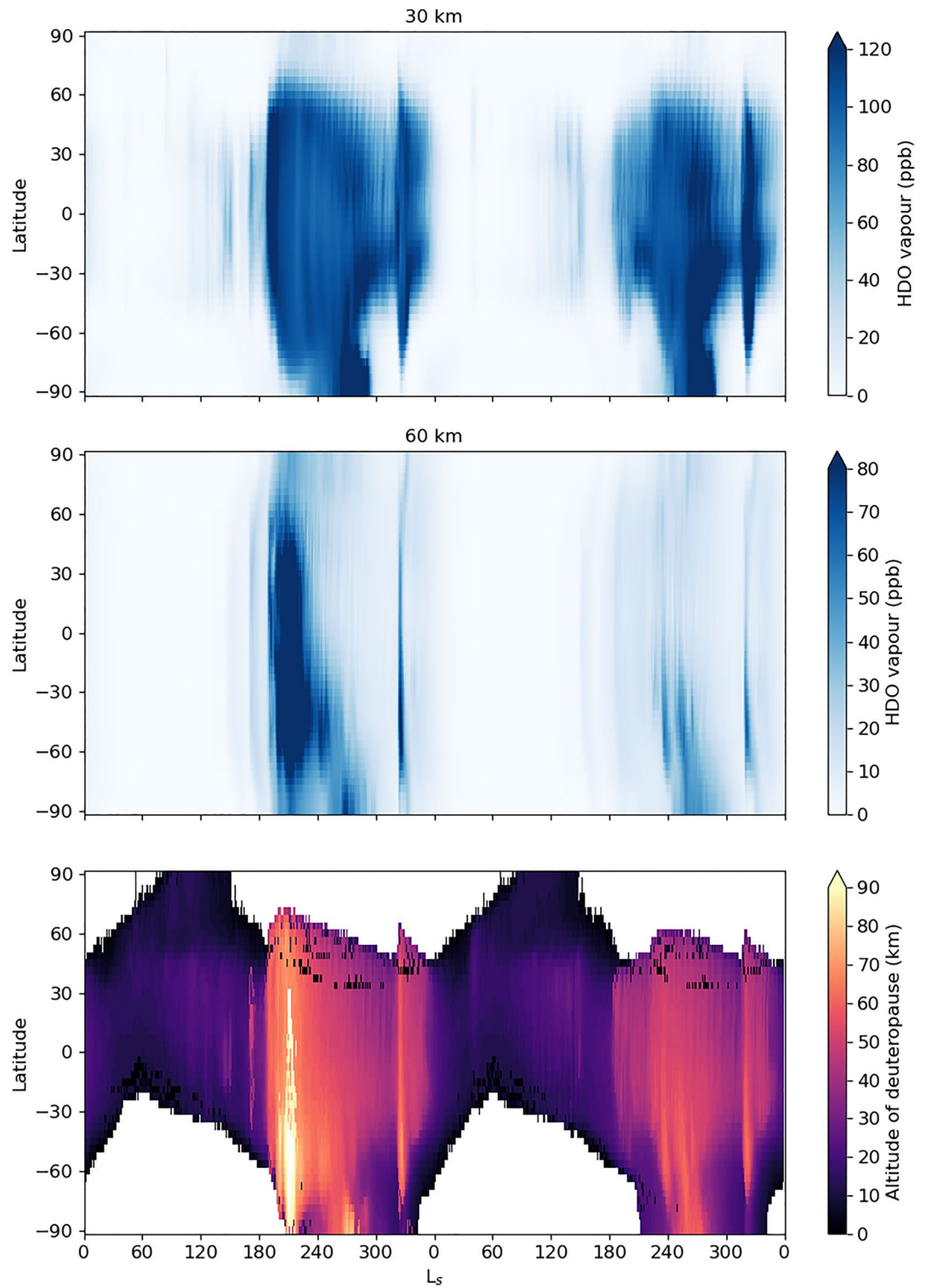


Figure 2. Seasonal cycle of the zonal average for HDO vapor at 30 km (top), HDO vapor at 60 km (middle) and the altitude of the deuteropause in km above the areoid (below), for MY34 and MY35. The altitude of the deuteropause is defined as the altitude below which $[HDO] < 50$ ppb. The deuteropause is therefore not defined if the whole profile is lower than 50 ppb.

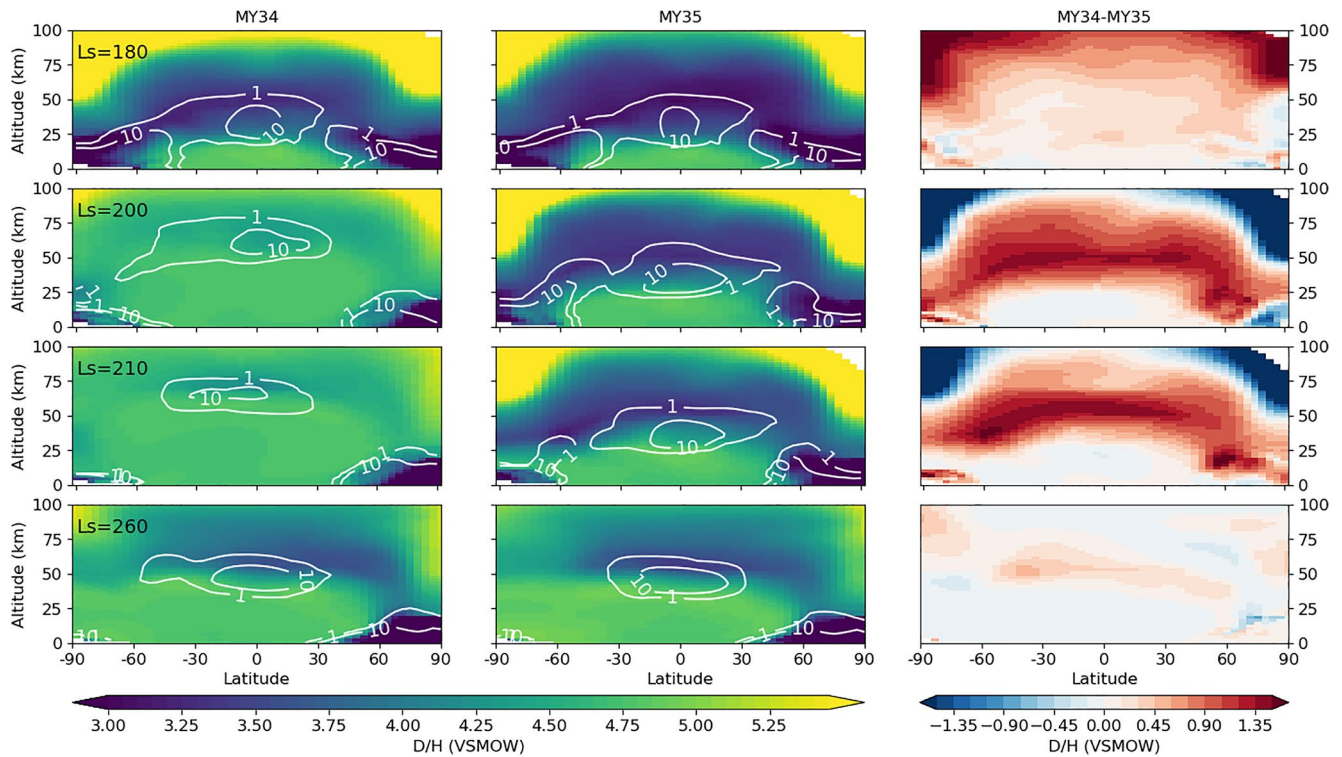


Figure 3. Meridional profile of the D/H ratio of the zonal average, for $L_s = 180, 200, 210, 260$ for MY34 and MY35 (left and center). The white contours indicate the mass mixing ratio of HDO ice in ppb. The last column shows the difference of the D/H ratio between MY34 and MY35.

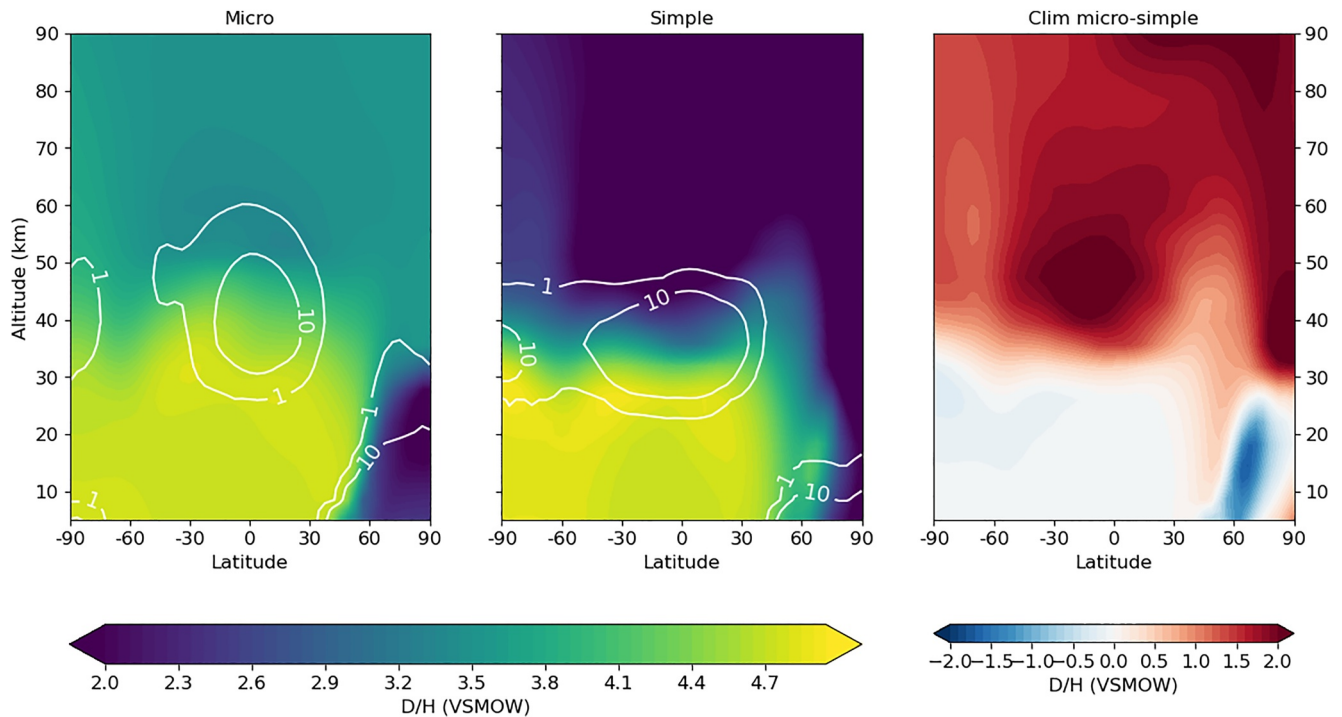


Figure 4. Meridional profile of the D/H ratio of the zonal average, temporally averaged over the $L_s \in [240^\circ - 270^\circ]$ period for the “climatology” scenario. The model presented here with the detailed microphysics of cloud formation and the radiative effect of clouds is shown on the left panel as “Micro,” the simplified model used in Rossi21 is shown in the middle as “Simple.” The white contours indicate the mass mixing ratio of HDO ice in ppb. The last column shows the difference of the D/H ratio between the two versions of the model.

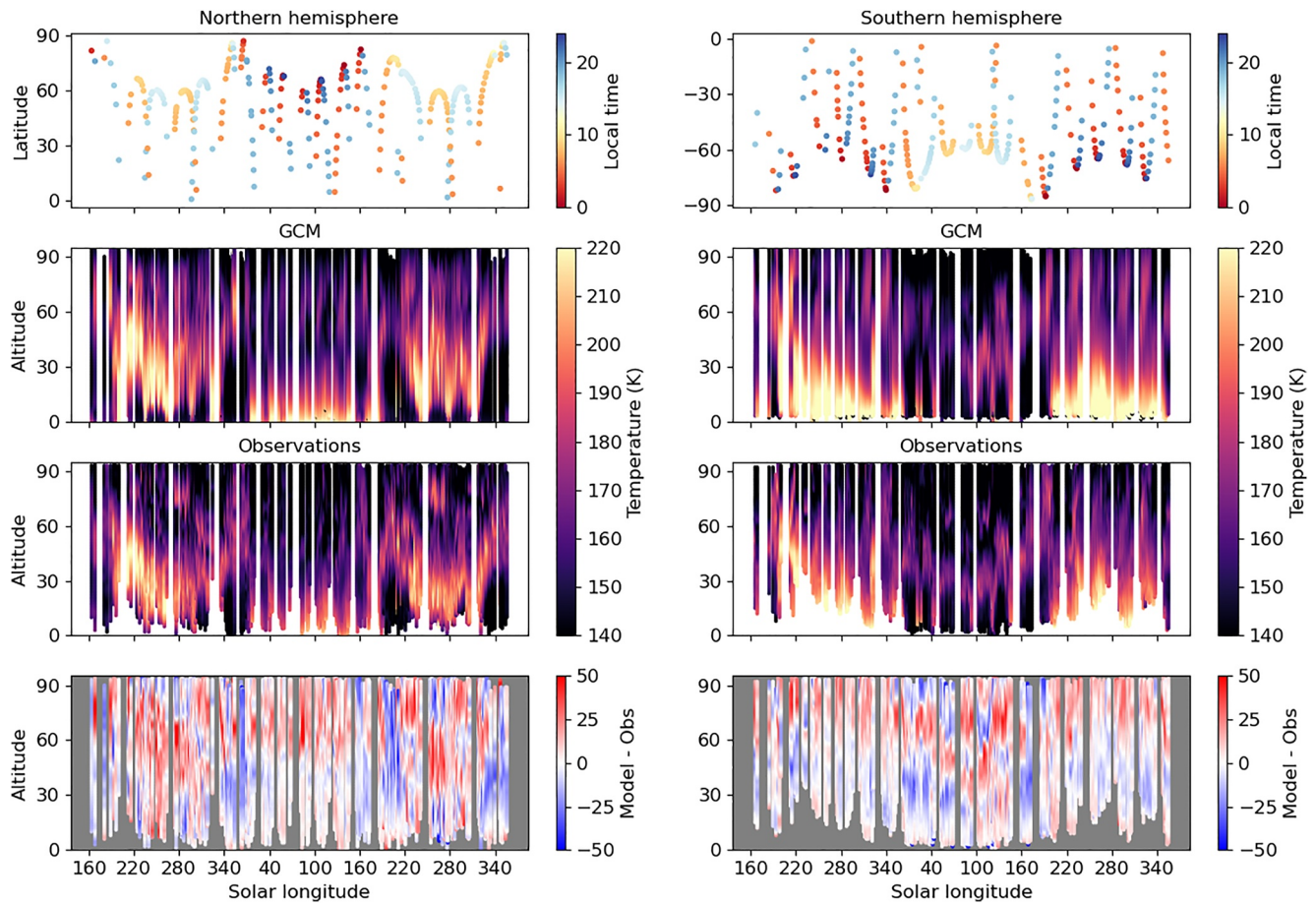


Figure 5. Comparison between model and data temperatures in the northern (left column) and southern (right) hemispheres, for MY34 (from $L_s = 160^\circ$) and MY35. The coordinates (latitude and solar longitude) of the observations are given in the top panels. The corresponding profiles are shown for the GCM (second line) and ACS (third line). The difference between the model and the observations is shown in the last line.

particular above 50 km at high latitudes ($>60^\circ$). In both hemispheres, the period $L_s = 180\text{--}250^\circ$ shows overall higher temperatures.

Regarding the water vapor, the model reproduces well the general trends (Figure 6). But it is also clear that the model is too wet at high altitudes, above 50 km, in the northern hemisphere. In the southern hemisphere, especially for MY35, the model is instead lacking water at these altitudes. Interestingly, this effect exists also for MY35, showing that it is not only due to the increased amount of dust in the atmosphere that occurred during MY34. In both years and both hemispheres, the dusty season shows the largest differences between the model and the observations in water vapor mixing ratio.

Finally we can look at the profiles for the D/H ratio (Figure 7). Due to the relative weakness of the HDO lines compared to the H_2O lines, the HDO mixing ratio is not always available concomitantly with the H_2O mixing ratio despite being measured simultaneously, explaining the sparse temporal and vertical coverage of the D/H ratio profiles. The observations and the model both show the seasonal variability with higher values of the D/H ratio during the perihelion season, in contrast to the aphelion season where the D/H ratio is usually lower and decreases more quickly with altitude. At high altitudes (above 75 km), the model shows an increase of the D/H ratio, with values above 6. This is the consequence of the photodissociation, which preferentially destroys H_2O over HDO and therefore tends to increase the D/H ratio, contrarily to condensation.

The difference between MY34 and MY35 is also apparent with higher values of the D/H ratio between $L_s = 160^\circ$ and 220° in MY34 than in MY35. This is true in the model, as seen earlier, but also the ACS observations, with HDO being detected at higher altitudes during this period in MY34 than in MY35. The difference between the

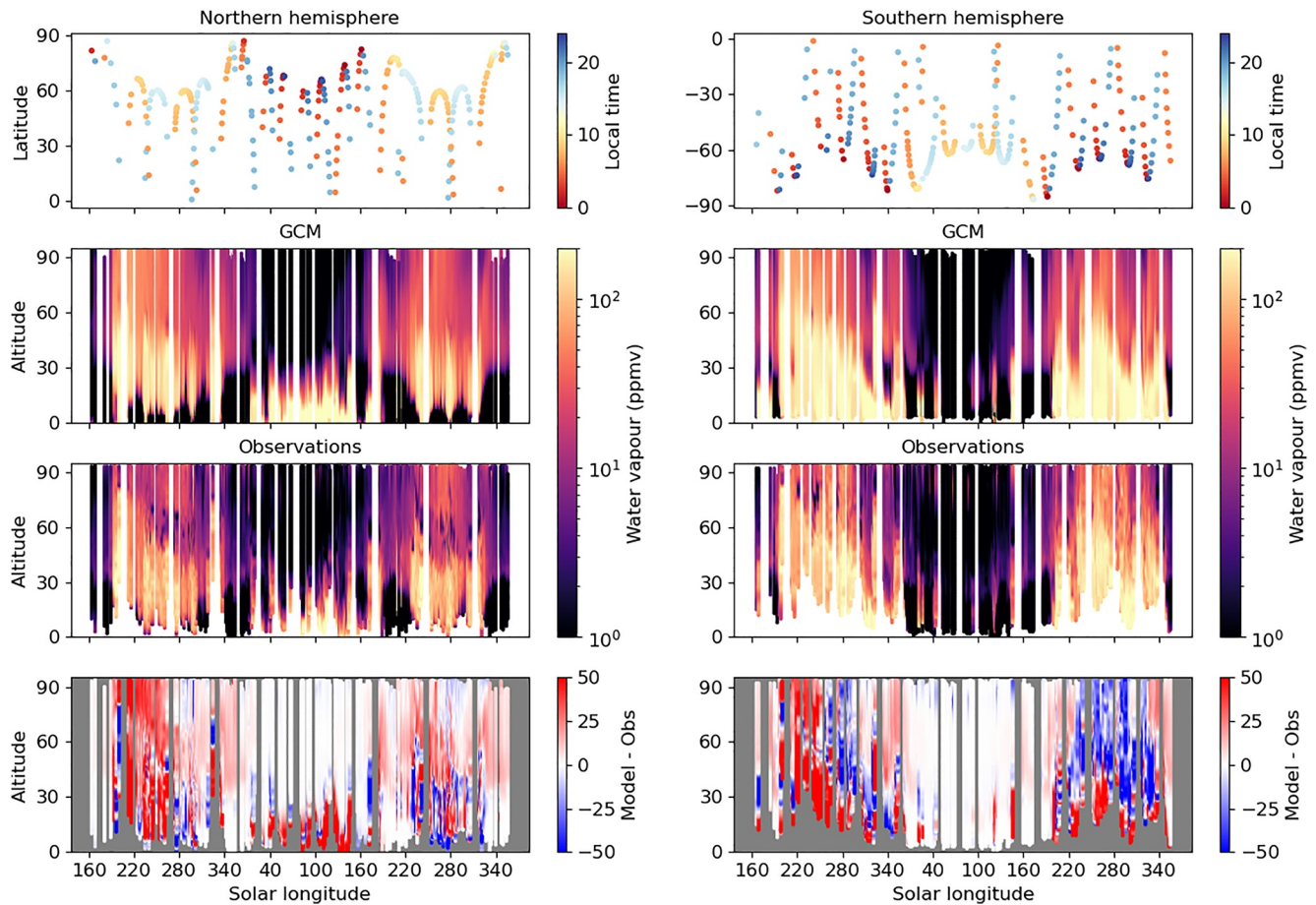


Figure 6. Same layout as Figure 5, but for the water vapor (in ppmv).

model and the observations shows an underestimation of the D/H ratio in the model in cases where the observed value is close to its maximum between 5 and 6. Around aphelion, where the observed values are lower, the model tends to overestimate the ratio.

Since the D/H ratio is mostly affected by the fractionation at condensation, it is interesting to look at the overall behavior of the D/H ratio with respect to the main drivers of the fractionation: the water vapor mixing ratio and the temperature. Figure 8 shows the distribution of values of D/H against the water vapor mixing ratio, for the observations and the model output. In both cases, the D/H ratio is globally lower at low values of water vapor. This is expected since the lower values of H₂O vapor are usually due to the condensation, which will reduce the D/H ratio through fractionation.

The same relation can be seen in Figure 9, this time with respect to temperature. Once again, the low temperatures are related to low values of the D/H ratio because these low temperatures are related to regions where fractionation has depleted the vapor phase of its HDO.

The figures also show the difference between the distributions from the GCM and the observations. The range of D/H values observed by ACS is larger than that from the GCM, even taking into account the observation bias, since the GCM values shown here are collocated with ACS observation coordinates, including regarding altitudes. While the ACS data and the GCM share a similar mean ratio (≈ 3.9), observations show a broader distribution. In particular, we note that the tail of the observed distribution extends to lower values than in the simulation, meaning that the model fails to reproduce low values of the D/H ratio in the altitude ranges probed by ACS-MIR.

There is also a difference in the slope of the distributions, especially in Figure 8. Since the D/H ratio depends on the temperature, the water mixing ratio and the saturation ratio, following Equation 3, the global relationship

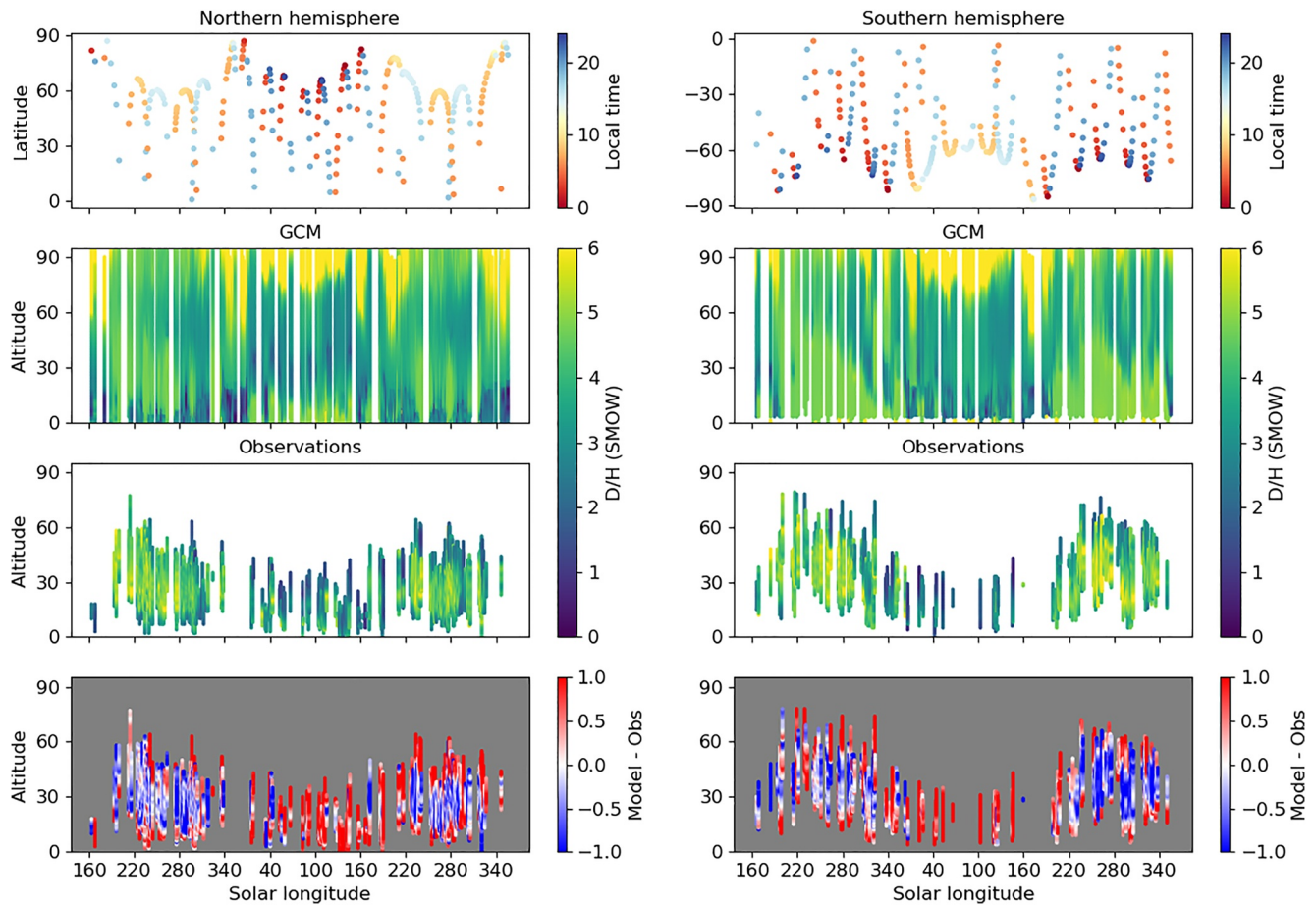


Figure 7. Same layout as Figure 5, but for the D/H ratio.

shown in Figures 8 and 9 can also depend on the saturation ratio and the coefficients used in the formula for the fractionation factor. In particular, it could be interesting to investigate possible deviations of the fractionation factor α in the martian conditions from the formula derived by Lamb et al. (2017), which was already an improvement over that of Merlivat and Nief (1967).

This difference between model and observations can be best addressed by considering individual profiles. For this comparison, we complete the HDO data set with retrievals of water ice mass loading by solar occultation from the ACS data. Methodology of aerosol properties retrieval as well as corresponding aerosol profiles retrieved from the combination of the TIRVIM and NIR spectra covering the period $L_s \in [170^\circ - 255^\circ]$ of MY 34 were published in Luginin et al. (2020). Here, together with previously published data we use additional TIRVIM and NIR aerosol profiles as well as completely new profiles retrieved from the combination of the MIR and NIR spectra (Figure 11, bottom).

In orbit 2556 (Figure 10, top), the simulated water profile is overall in agreement with the observations. But the observed temperatures present oscillations that are not reproduced by the model. This and the misrepresentation of the ice content between 10 and 30 km lead to variations of the D/H ratio not reproduced by the model.

For the orbit 3513 (Figure 10, middle) the water vapor below 50 km, while overestimated by the model, is not observed to be fractionated, thus the D/H ratio below the cloud level is well reproduced by the model. On the other hand, the condensation level is poorly represented, with a much sharper decrease of water vapor around 55 km in the observations. This is consistent with the underestimation of the ice content by the model, leaving the upper atmosphere with too much water vapor in a supersaturated state. As a consequence the fractionation is incorrect and the D/H ratio above 50 km no longer matches the observation.

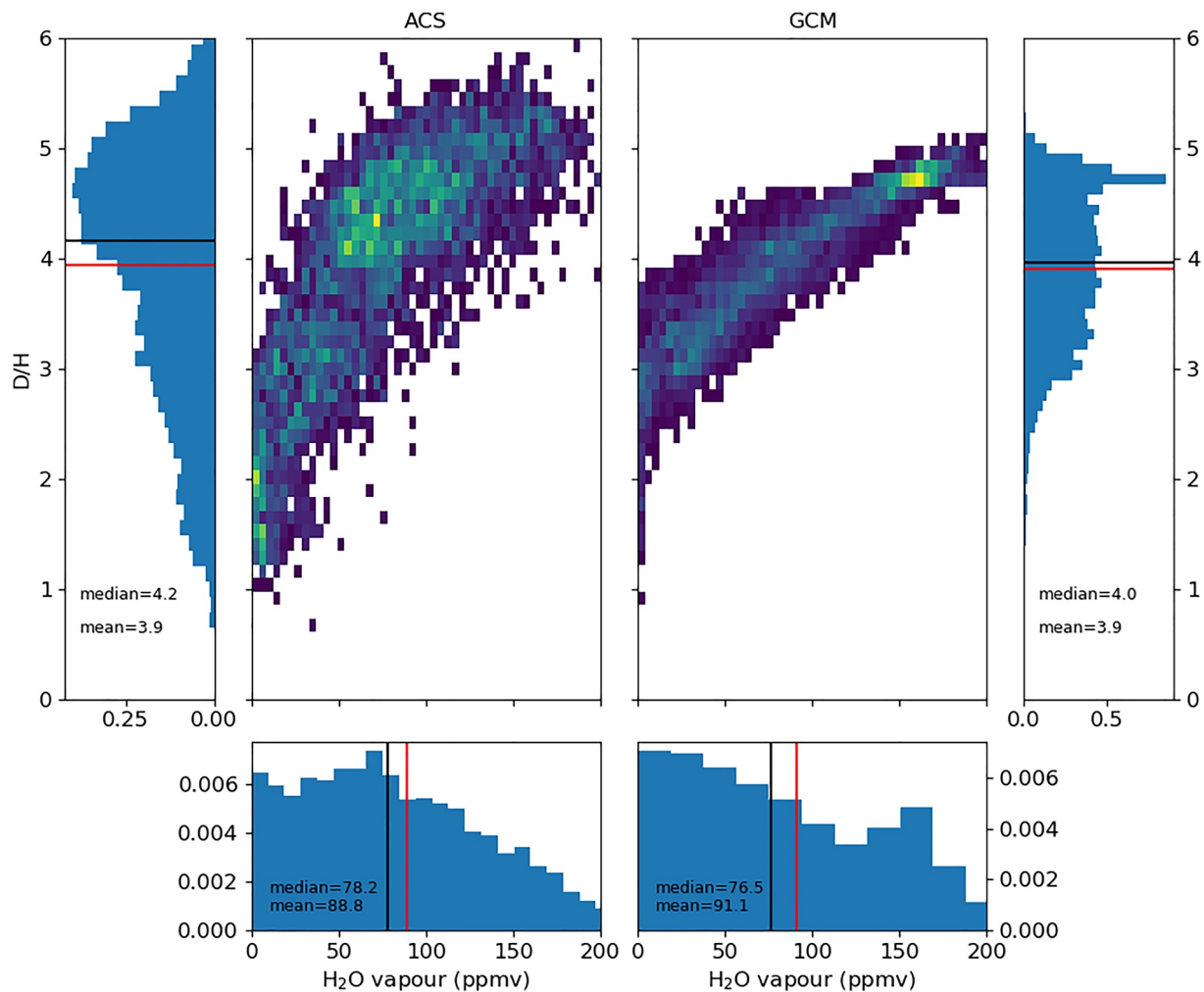


Figure 8. 2D histogram of the values of the D/H ratio against the water vapor mixing ratio. The marginal normalized distributions are visible on the sides, with a black line showing the median and a red line showing the mean. The left panels show the distributions for the ACS observations. The right panels are for colocated GCM simulations.

A similar issue occurs with orbit 12059 (Figure 11, bottom) where the profiles for water agree up to 40 km, above which the model sees a decrease in water vapor. In the observed profile, the hygropause occurs higher, around 55 km. Once again, the comparison between the modeled and observed ice profiles shows that the model underestimates the amount of ice above 50 km and consequently the amount of condensation-induced fractionation. This explains the sharp decrease of the D/H ratio observed by ACS, but not reproduced by the model. Another example of this, but in a different season and latitude is given by orbit 8401 (Figure 11, middle) where the ice observed between 20 and 40 km is not predicted by the model, which therefore cannot predict the sharp decrease of the isotopic ratio in the same altitude range.

In orbit 4409 (Figure 10, bottom), the D/H values before and after the deuteropause are relatively well reproduced, but the location of the hygropause is incorrectly located around 30 km in the model, instead of the observed 45 km. In this case the cloud formation seems to occur higher in the observations (maximum of ice around 60 km) than in the model (maximum around 50 km). The ice mass load is also higher in the observations. This leads to a higher hygropause and a higher deuteropause than in the model.

Orbit 6844 (Figure 11, top) shows a case in the polar region where the model overestimates the amount of ice below 20 km. This lead to a model drier than the observations and to a stronger fractionation which explains why the ratio predicted by the model is lower than that of the observations.

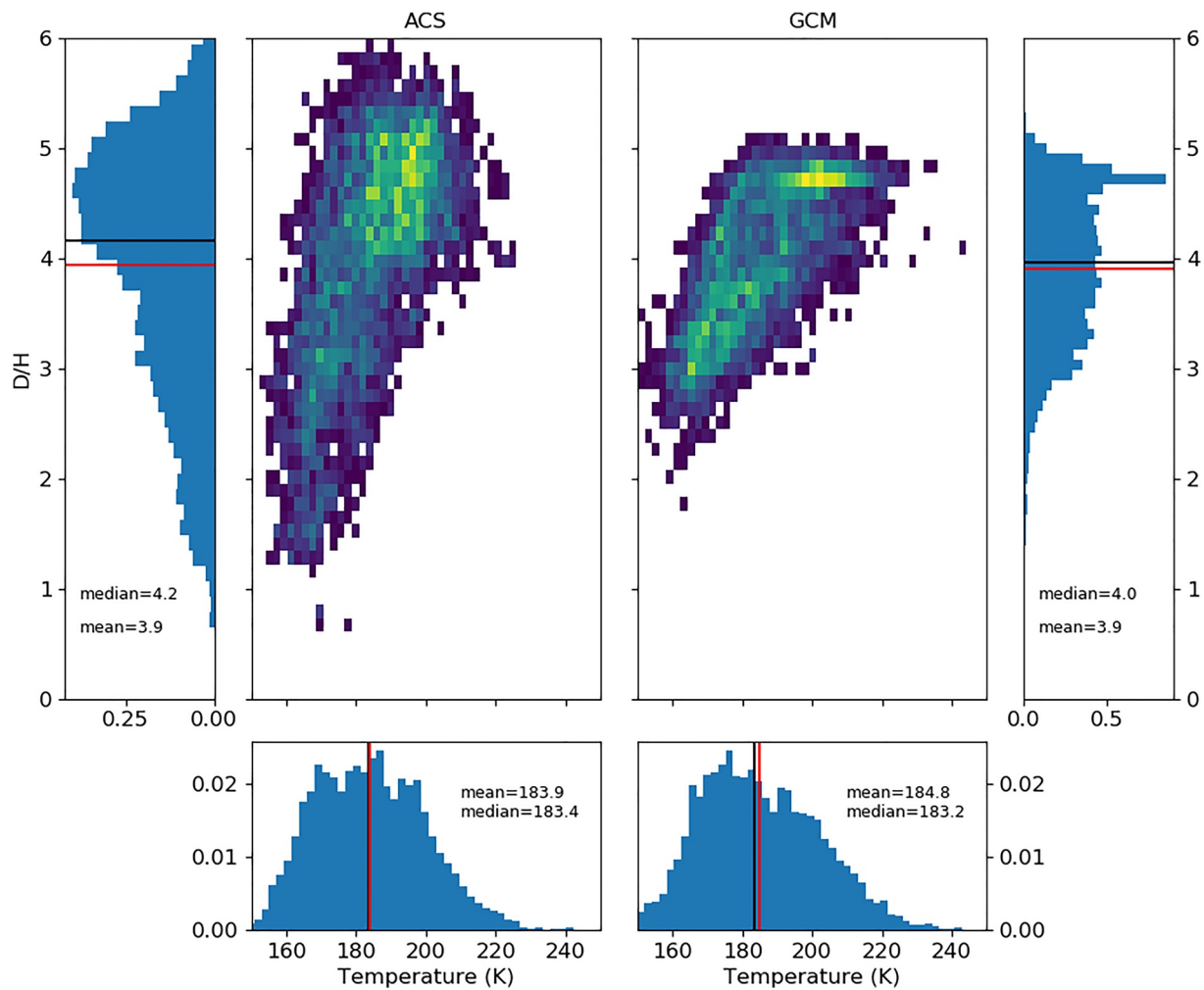


Figure 9. Same layout as Figure 8, but for the temperature.

In order to compensate the irregular temporal and spatial (notably vertical) sampling in the data and to investigate better the seasonal variations, we averaged the observed and collocated GCM profiles in bins of latitude and of months, as in Figure 12.

We can start by comparing the ACS profiles from MY34 and MY35. In particular, the profiles corresponding to the GDS show higher values of the D/H ratio in MY34 than in MY35, with the isotopic ratio decreasing only at higher altitudes, as already identified previously (Alday et al., 2021; Vandaele et al., 2019).

It is also interesting to note that the global mean of the GCM (red curves) follows closely the mean of the collocated GCM profiles, with a few exceptions of the polar areas. This indicates that the observational sampling of ACS is representative of the conditions of the atmosphere for the bins considered. In the polar regions, the sampling in local-time could explain the differences.

The model shows a good qualitative agreement, successfully capturing the trend in the vertical evolution of the D/H ratio, in particular at mid- and equatorial latitudes, but less so in the polar regions.

During the perihelion season, the model is in quantitative agreement with the observations in the middle atmosphere, with similar maximal values of the D/H ratio. But during the aphelion season of MY35, the model predicts a much higher value of the D/H ratio in the polar regions, despite the vertical trend being reproduced. As seen in Figure 5, the model tends to overestimate the amount of water vapor in this time period, in particular in the northern hemisphere. This excess water vapor, associated with a lack of ice at low altitudes, could explain the discrepancy. Processes linked to the surface ice could also play a role and would need further exploration.

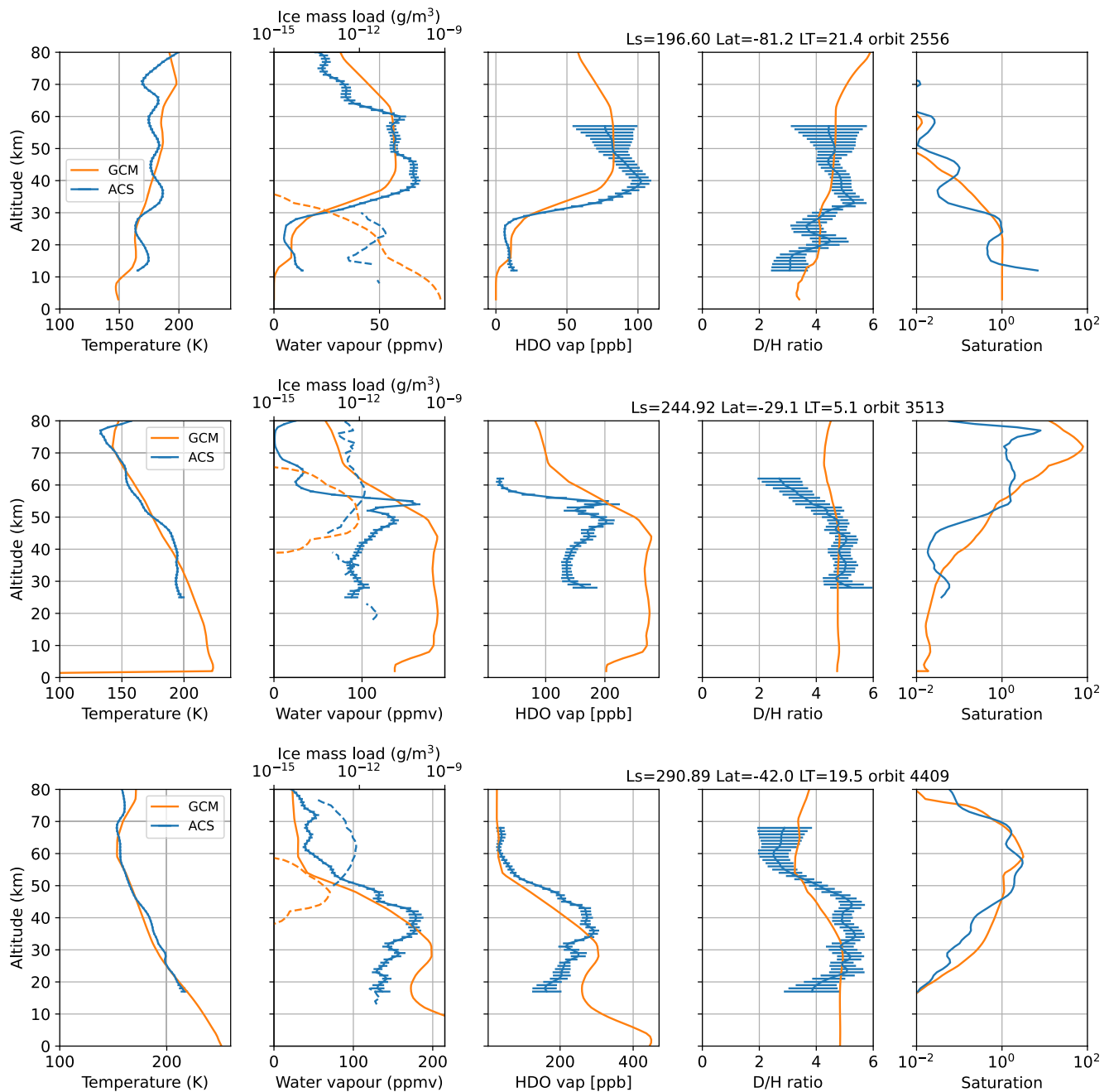


Figure 10. Profiles of temperature, water vapor, water ice mass loading, HDO vapor, D/H ratio and saturation ratio, for ACS observations and GCM collocated simulations. Here are shown orbits 2556, 3513 and 4409. The dashed lines in the second panel show collocated ACS water ice mass loading retrievals.

In general the model seems to fail to represent the observed decrease of the D/H ratio above 50 km and closer to the surface. It seems that the model does not reproduce the amplitude of the variation of the D/H ratio with altitude, suggesting that while the processes are understood, their efficiency might be lower than what is needed.

A likely explanation for this discrepancy is the insufficient condensation at high altitudes or close to the surface. This is visible in Figures 10 and 11, but is also apparent in Figure 13 where observed and simulated profiles of temperature, water ice, water vapor and D/H ratio are presented, averaged over the period $L_s \in [240^\circ\text{--}300^\circ]$ of MY34 and latitude range $[-45^\circ\text{ to }45^\circ]$. The model does not predict enough ice in the 10–20 km range, which would lead to an underestimation of the fractionation. As a result, the model doesn't reproduce the decrease of the

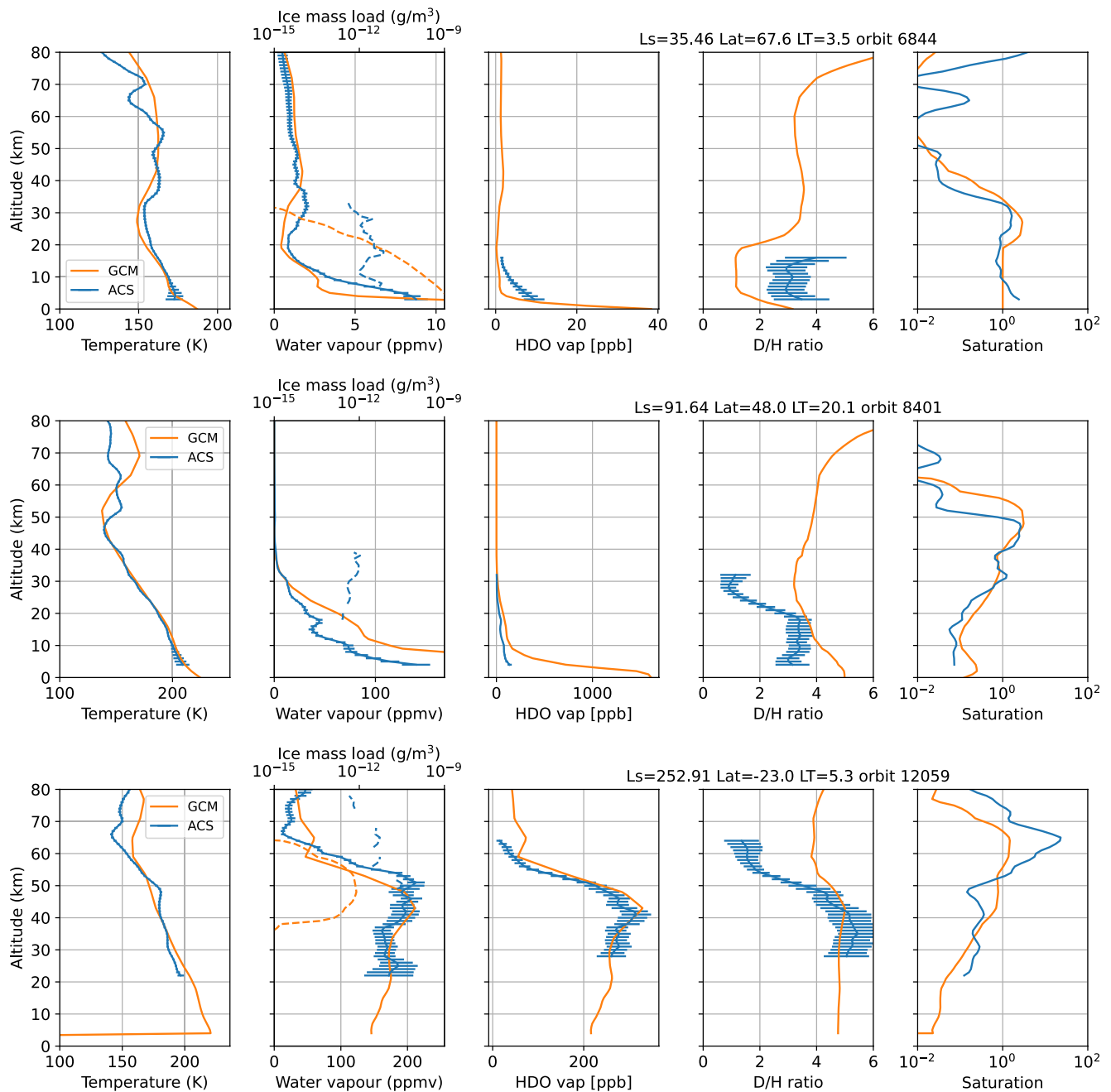


Figure 11. Profiles of temperature, water vapor, water ice mass loading, HDO vapor, D/H ratio and saturation ratio, for ACS observations and GCM collocated simulations. Here are shown orbits 6844, 8401 and 12059. The dashed lines in the second panel show collocated ACS water ice mass loading retrievals.

D/H ratio close to the surface. At high altitudes, a similar issue is observed with a lack of ice above 60 km. This ice at high altitude explains the sharp decrease of the D/H ratio above 60 km, which the model cannot reproduce.

This would be consistent with the excessive values of supersaturation seen in the model, and with the lack of dust at high altitude (cf. companion paper for a more detailed discussion on that aspect). With less dust being available to act as CCN, ice particles cannot form, leaving the upper atmosphere supersaturated with respect to ice. Since the fractionation by condensation is the main factor controlling the isotopic ratio, less condensation leads to higher values of the D/H ratio at these altitudes.

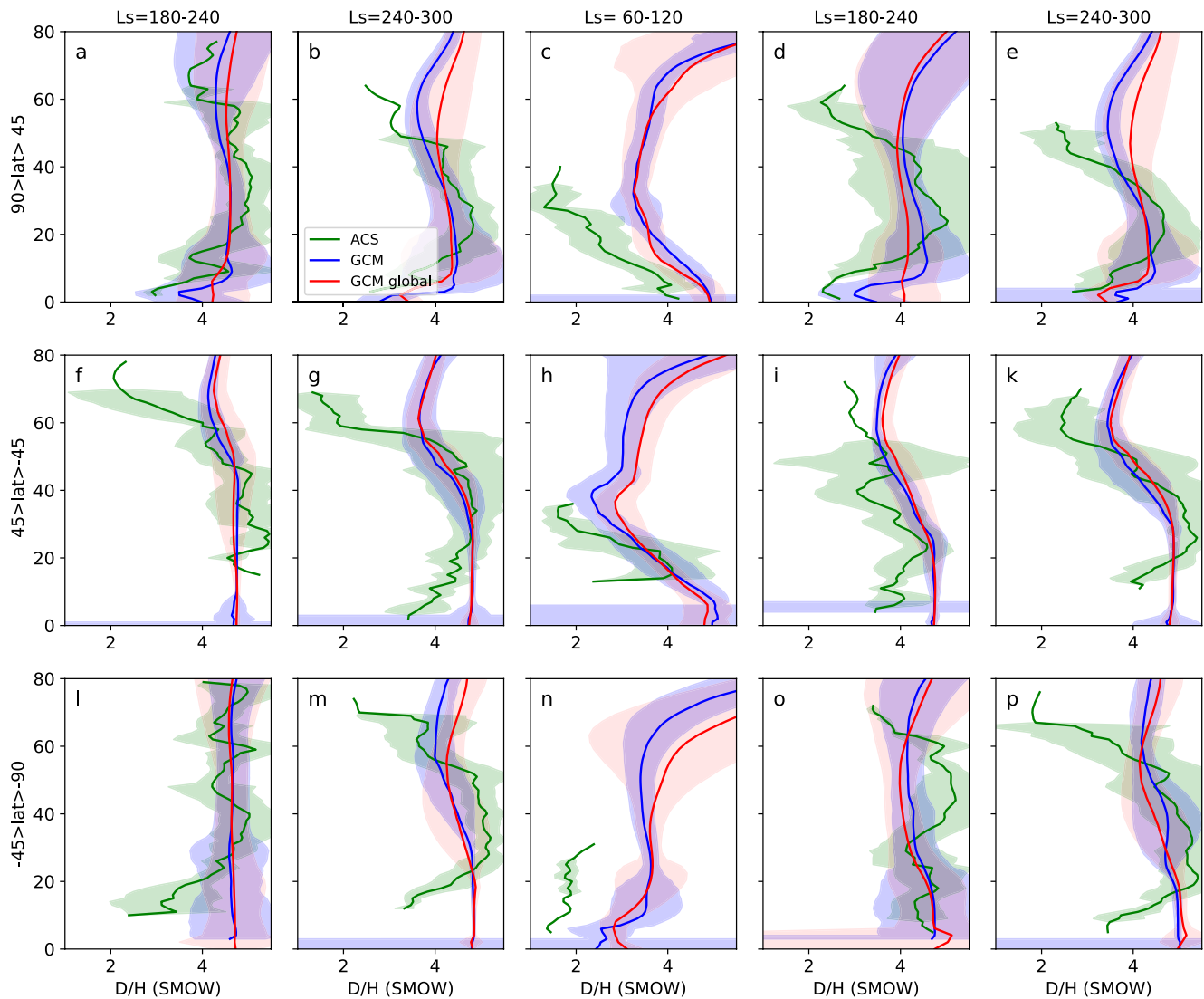


Figure 12. Binned values of D/H ratio for selected time ranges in MY34 (left panels, a, b, f, g, l and m) and MY35 (right panels). The profiles are averaged by latitude bins: high latitudes ($|\phi| > 45^\circ$), mid-equatorial latitudes ($|\phi| < 45^\circ$). They are also averaged by periods of L_s . The green curves show the ACS profiles averaged with weights based on the errors and the amount of water vapor. The blue curves represent the collocated GCM profiles, weighted by the amount of water vapor. The red curves represent the overall average GCM profiles, over the whole bin, providing an indication of the bias due to the spatial and temporal sampling in the observations. For all curves, the shaded area corresponds to the standard deviation of the profiles in the bin.

5. Discussion

As illustrated by the individual and averaged profiles, the GCM performs essentially well in reproducing the general trends of variation of the D/H ratio. This reflects the capacity of the model to reproduce the condensation and the related fractionation. This in turn, relies on the model correctly representing the temperature profile and the conditions of condensation, in particular the amount of dust available to act as CCN. The difficulties of the model to reproduce the condensation occurring at high altitude likely explain why the distributions of D/H shown in Figure 8 differ regarding the lower values, with a larger number of instances of D/H ratios below two in the observations. These low values correspond to a heavy fractionation, and therefore to a strong condensation.

The detailed microphysics of the condensation and the inclusion of the radiative effect of clouds improves significantly the simulations when compared with the model used in Rossi21. In Figure 13, both the model with the detailed physics (“Micro”) and the simplified scheme from Rossi21 (“simple”) are shown. The “Micro” model

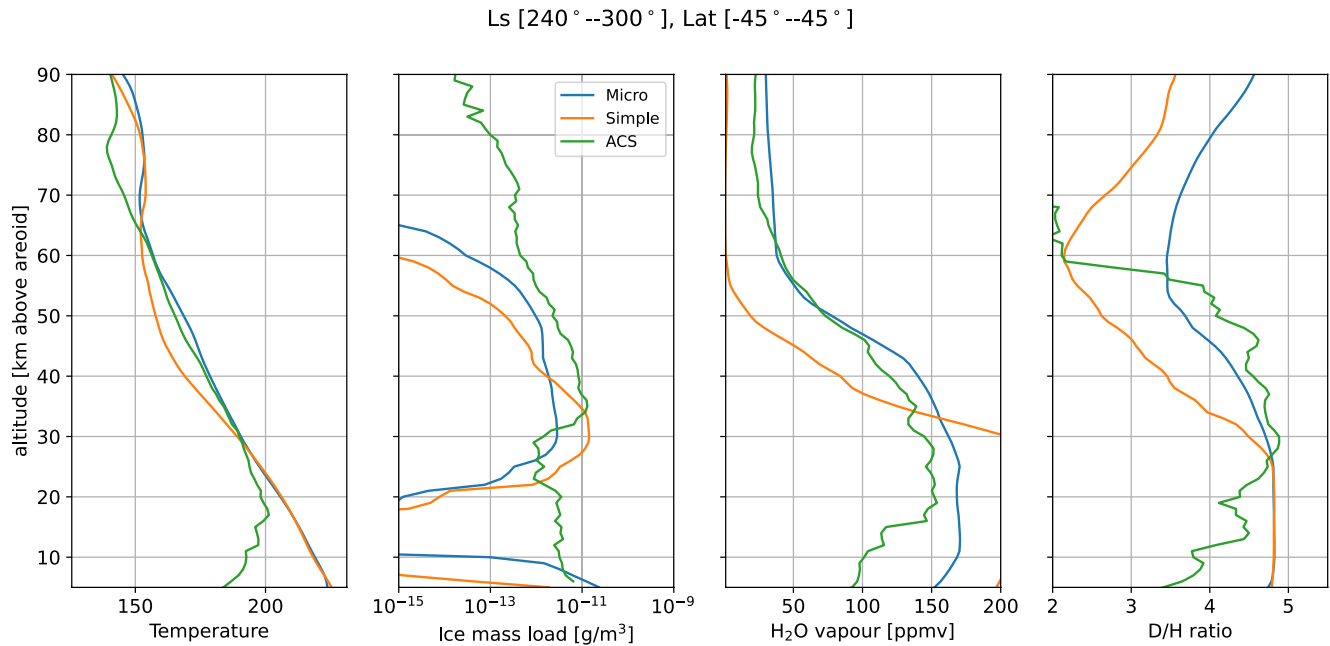


Figure 13. Averaged profiles of the ice mass load, water volume mixing ratio, D/H ratio and temperature for the period $L_s \in [240^\circ\text{--}300^\circ]$ and latitude range $[-45^\circ$ to $45^\circ]$ —(corresponding to Figure 12g). Both colocated GCM and data from ACS are shown. For the GCM profiles, both the version with the detailed cloud microphysics and the simplified scheme are shown.

used in this study improves significantly the water cycle (as discussed in more details in the companion paper), and it is a clear improvement on the D/H ratio as well.

The main limitation of the improved model seems to be a correct representation of the condensation, in particular the lack thereof. This can be related to possible issues in the speed of the condensation, once nucleation is initiated. But the lack of dust to act as CCN would also strongly limit the formation of ice particles. This is a known problem in the GCM, which is unable to transport dust to high altitudes, creating a lack of condensation nuclei at high altitude.

A logical consequence of the lack of condensation at high altitudes, is the supersaturation which, as illustrated by the companion paper, also plays an important role. First because it has an impact on the porosity of the deuteropause, thus increasing the amount of water vapor and reducing the condensation. Second because the inclusion of the effect of kinetics means that the fractionation factor depends on the saturation ratio. Therefore supersaturation will tend to further decrease the efficiency of the fractionation.

Another limitation of this study is the limited vertical range where HDO is reliably measured and can be compared to the model. Only a few profiles reach altitudes above 50–60 km, where the porosity of the deuteropause controls the D/H ratio, making difficult to understand what happens to HDO itself, beyond what we can see from H_2O alone.

6. Conclusion

We have used a GCM of Mars to simulate the HDO cycle. The model includes realistic representation of the microphysics of cloud formation, the radiative effect of clouds and the photochemistry.

We have compared the model simulations with solar occultation data from the MIR channel of the Atmospheric Chemistry Suite, on board the TGO. The model shows a good qualitative agreement with the observations, successfully capturing the effects of condensation-induced fractionation, which appears to be the main factor controlling the D/H ratio. The misrepresentation of condensation appears to be the main cause of disagreement in the D/H ratio between the model and the data. The known issues in the transport of dust particles at high altitude by the model are a likely cause of misrepresentation of the condensation, although not the only one.

Improvements in the representation of the water and dust cycles in the LMD Mars GCM are on-going, and are expected to lead to improvements in the representation of related physical processes, such as the isotopic ratios and the HDO cycle.

The recent implementation of the escape of deuterium in the model could provide material for further studies involving MAVEN data, and on the study of the escape of water vapor on Mars.

Data Availability Statement

The data used to produce the figures in this study are available from Rossi and Vals (2022). The HDO retrievals used in this study were initially published in Alday et al. (2021) and the data can be obtained from Alday (2021). The water ice retrievals were initially published in Luginin et al. (2020) and can be obtained from Luginin (2020). The LMD GCM is freely available from the dedicated subversion online server <http://svn.lmd.jussieu.fr/Planeto/trunk>, which includes a user manual (http://svn.lmd.jussieu.fr/Planeto/trunk/LMDZ.MARS/user_manual.pdf). This work was done using revision 2593 of the GCM.

Acknowledgments

L.R. acknowledges support from CNES. F.G.-G. is funded by the Spanish Ministerio de Ciencia, Innovación y Universidades, the Agencia Estatal de Investigación and EC FEDER funds under project RTI2018-100920-J-I00, and acknowledges financial support from the State Agency for Research of the Spanish MCIU through the “Center of Excellence Severo Ochoa” award to the Instituto de Astrofísica de Andalucía (SEV-2017-0709). M.V. acknowledges support from the DIM ACAV labelled by the Ile-de-France region in support for the research (“Domaine d’Intérêt Majeur, Astrophysique et Conditions d’Apparition de la Vie.”)

References

- Alday, J. (2021). Isotopic composition of H₂O and CO₂ on Mars from acs mir solar occultations (version v01) [Dataset]. Zenodo. <https://doi.org/10.5281/ZENODO.5100448>
- Alday, J., Trokhimovskiy, A., Irwin, P. G., Wilson, C. F., Montmessin, F., Lefèvre, F., et al. (2021). Isotopic fractionation of water and its photolytic products in the atmosphere of Mars. *Nature Astronomy*, 5(9), 1–8. <https://doi.org/10.1038/s41550-021-01389-x>
- Bertaux, J.-L., & Montmessin, F. (2001). Isotopic fractionation through water vapor condensation: The deuteropause, a cold trap for deuterium in the atmosphere of Mars. *Journal of Geophysical Research*, 106(E12), 32879–32884. Retrieved from <https://agupubs.onlinelibrary.wiley.com/doi/abs/10.1029/2000JE001358>
- Cheng, B.-M., Chung, C.-Y., Bahou, M., Lee, Y.-P., Lee, L. C., van Harreveld, R., & van Hemert, M. C. (2004). Quantitative spectroscopic and theoretical study of the optical absorption spectra of H₂O, HOD, and D₂O in the 125–145 nm region. *Journal of Chemical Physics*, 120(1), 224–229. <https://doi.org/10.1063/1.1630304>
- Chung, C.-Y., Chew, E. P., Cheng, B.-M., Bahou, M., & Lee, Y.-P. (2001). Temperature dependence of absorption cross-section of H₂O, HOD, and D₂O in the spectral region 140–193 nm. *Nuclear Instruments and Methods in Physics Research Section A: Accelerators, Spectrometers, Detectors and Associated Equipment*, 467(2002), 1572–1576. [https://doi.org/10.1016/S0168-9002\(01\)00762-8](https://doi.org/10.1016/S0168-9002(01)00762-8)
- Daerden, F., Neary, L., Villanueva, G., Liuzzi, G., Aoki, S., Clancy, R. T., et al. (2022). Explaining nomad d/h observations by cloud-induced fractionation of water vapor on Mars. *Journal of Geophysical Research: Planets*, 127(2), e2021JE007079. Retrieved from <https://agupubs.onlinelibrary.wiley.com/doi/abs/10.1029/2021JE007079>
- Forget, F., Hourdin, F., Fournier, R., Hourdin, C., Talagrand, O., Collins, M., et al. (1999). Improved general circulation models of the martian atmosphere from the surface to above 80 km. *Journal of Geophysical Research*, 104(E10), 24155–24175. <https://doi.org/10.1029/1999je001025>
- Fouchet, T., & Lellouch, E. (2000). Vapor pressure isotope fractionation effects in planetary atmospheres: Application to deuterium. *Icarus*, 144(1), 114–123. Retrieved from <http://www.sciencedirect.com/science/article/pii/S001910359962644>
- Jouzel, J., & Merlivat, L. (1984). Deuterium and oxygen 18 in precipitation: Modeling of the isotopic effects during snow formation. *Journal of Geophysical Research*, 89(D7), 11749–11757. <https://doi.org/10.1029/jd089id07p11749>
- Korablev, O., Montmessin, F., Trokhimovskiy, A., Fedorova, A. A., Shakun, A. V., Grigoriev, A. V., et al. (2018). The atmospheric chemistry suite (ACS) of three spectrometers for the ExoMars 2016 trace gas orbiter. *Space Science Reviews*, 214(1), 7. Retrieved 2020-08-10, from <http://link.springer.com/10.1007/s11214-017-0437-6>
- Lamb, K. D., Clouser, B. W., Bolot, M., Sarkozy, L., Ebert, V., Saathoff, H., et al. (2017). Laboratory measurements of HDO/H₂O isotopic fractionation during ice deposition in simulated cirrus clouds. In *Proceedings of the national academy of sciences* (Vol. 114, pp. 5612–5617). Retrieved from <https://www.pnas.org/content/114/22/5612>
- Lefèvre, F., Trokhimovskiy, A., Fedorova, A., Baggio, L., Lacombe, G., Määttä, A., et al. (2021). Relationship between the ozone and water vapor columns on Mars as observed by spicam and calculated by a global climate model. *Journal of Geophysical Research: Planets*, 126(4), e2021JE006838. Retrieved from <https://agupubs.onlinelibrary.wiley.com/doi/abs/10.1029/2021JE006838>
- Luginin, M. (2020). Aerosols from acs during 2018 gds [Dataset]. Mendeley. <https://doi.org/10.17632/RKSZDMPDCY.1>
- Luginin, M., Fedorova, A., Ignatiev, N., Trokhimovskiy, A., Shakun, A., Grigoriev, A., et al. (2020). Properties of water ice and dust particles in the atmosphere of Mars during the 2018 global dust storm as inferred from the atmospheric chemistry suite. *Journal of Geophysical Research: Planets*, 125(11), e2020JE006419. Retrieved from <https://agupubs.onlinelibrary.wiley.com/doi/abs/10.1029/2020JE006419>
- Madeleine, J.-B., Forget, F., Millour, E., Montabone, L., & Wolff, M. J. (2011). Revisiting the radiative impact of dust on Mars using the lmd global climate model. *Journal of Geophysical Research*, 116(E11), E11010. Retrieved from <https://agupubs.onlinelibrary.wiley.com/doi/abs/10.1029/2011JE003855>
- Madeleine, J.-B., Forget, F., Millour, E., Navarro, T., & Spiga, A. (2012). The influence of radiatively active water ice clouds on the martian climate. *Geophysical Research Letters*, 39(23). Retrieved from <https://agupubs.onlinelibrary.wiley.com/doi/abs/10.1029/2012GL053564>
- Merlivat, L., & Nief, G. (1967). Fractionnement isotopique lors des changements d'état solide-vapeur et liquide-vapeur de l'eau à des températures inférieures à 0°C. *Tellus*, 19(1), 122–127. Retrieved from <https://onlinelibrary.wiley.com/doi/abs/10.1111/j.2153-3490.1967.tb01465.x>
- Montabone, L., Forget, F., Millour, E., Wilson, R., Lewis, S., Cantor, B., et al. (2015). Eight-year climatology of dust optical depth on Mars. *Icarus*, 251, 65–95. (Dynamic Mars). <https://doi.org/10.1016/j.icarus.2014.12.034>
- Montabone, L., Spiga, A., Kass, D. M., Kleinböhl, A., Forget, F., & Millour, E. (2020). Martian year 34 column dust climatology from Mars climate sounder observations: Reconstructed maps and model simulations. *Journal of Geophysical Research: Planets*, 125(8), e2019JE006111. Retrieved from <https://agupubs.onlinelibrary.wiley.com/doi/abs/10.1029/2019JE006111>
- Montmessin, F., Forget, F., Rannou, P., Cabane, M., & Haberle, R. (2004). Origin and role of water ice clouds in the martian water cycle as inferred from a general circulation model. *Journal of Geophysical Research*, 109(E10), E10004. <https://doi.org/10.1029/2004je002284>

- Montmessin, F., Fouchet, T., & Forget, F. (2005). Modeling the annual cycle of HDO in the martian atmosphere. *Journal of Geophysical Research*, *110*(E3). Retrieved from <https://agupubs.onlinelibrary.wiley.com/doi/abs/10.1029/2004JE002357>
- Navarro, T., Madeleine, J.-B., Forget, F., Spiga, A., Millour, E., Montmessin, F., & Määttä, A. (2014). Global climate modeling of the martian water cycle with improved microphysics and radiatively active water ice clouds. *Journal of Geophysical Research: Planets*, *119*(7), 1479–1495. Retrieved from <https://agupubs.onlinelibrary.wiley.com/doi/abs/10.1002/2013JE004550>
- Neary, L., Daerden, F., Aoki, S., Whiteway, J., Clancy, R., Smith, M., et al. (2020). Explanation for the increase in high-altitude water on Mars observed by nomad during the 2018 global dust storm. *Geophysical Research Letters*, *47*(7), e2019GL084354. <https://doi.org/10.1029/2019gl084354>
- Risi, C., Bony, S., Vimeux, F., & Jouzel, J. (2010). Water-stable isotopes in the lmdz4 general circulation model: Model evaluation for present-day and past climates and applications to climatic interpretations of tropical isotopic records. *Journal of Geophysical Research*, *115*(D12), D12118. <https://doi.org/10.1029/2009jd013255>
- Rossi, L., & Vals, M. (2022). Comparisons of the simulated martian HDO cycle with the upgraded lmd Mars gem [Dataset]. ESPRI/IPSL. <https://doi.org/10.14768/11F03207-0FC7-4784-BBDB-EECAE34E6C32>
- Rossi, L., Vals, M., Montmessin, F., Forget, F., Millour, E., Fedorova, A., et al. (2021). The effect of the martian 2018 global dust storm on HDO as predicted by a Mars global climate model. *Geophysical Research Letters*, *48*(7), e2020GL090962. Retrieved from <https://agupubs.onlinelibrary.wiley.com/doi/abs/10.1029/2020GL090962>
- Vals, M., Rossi, L., Montmessin, F., Lefèvre, F., Gonzalez-Galindo, F., Fedorova, A., et al. (2022). Improved modeling of Mars' HDO cycle using a Mars' Global Climate Model. *Journal of Geophysical Research: Planets*, *127*, e2022JE007192. <https://doi.org/10.1029/2022JE007192>
- Vandaele, A. C., Korabev, O., Daerden, F., Aoki, S., Thomas, I. R., Altieri, F., et al. (2019). Martian dust storm impact on atmospheric H₂O and d/h observed by exomars trace gas orbiter. *Nature*, *568*(7753), 521–525.
- Vandaele, A. C., Patel, M. R., Bellucci, G., Daerden, F., Ristic, B., Robert, S., et al. (2018). NOMAD, an integrated suite of three spectrometers for the ExoMars trace gas mission: Technical description, science objectives and expected performance. *Space Science Reviews*, *214*(5), 80. Retrieved 2020-08-10, from <http://link.springer.com/10.1007/s11214-018-0517-2>
- Villanueva, G. L., Mumma, M. J., Novak, R. E., Käufel, H. U., Hartogh, P., Encrenaz, T., et al. (2015). Strong water isotopic anomalies in the martian atmosphere: Probing current and ancient reservoirs. *Science*, *348*(6231), 218–221. <https://doi.org/10.1126/science.aaa3630>